

Spatio-Temporal Forecasting of Retaining Wall Deformation: Mitigating Error Accumulation via Multi-Resolution ConvLSTM Stacking Ensemble

Jihoon Kim^{1a}, Heejung Youn^{1*}

¹Department of Civil and Environmental Engineering, Hongik University, Seoul, Republic of Korea

Abstract. This study proposes a multi-resolution Convolutional Long Short-Term Memory (ConvLSTM) ensemble framework that leverages diverse temporal input resolutions to mitigate error accumulation and improve long-horizon forecasting of retaining-structure behavior during staged excavation. An extensive database of lateral wall displacement responses was generated through PLAXIS2D simulations incorporating five-layered soil stratigraphy, two excavation depths (14 and 20 m), and stochastically varied geotechnical and structural parameters, yielding 2,000 time-series deflection profiles. Three ConvLSTM models trained at different input resolutions were integrated using a fully connected neural network meta-learner to construct the ensemble model. Validation using both numerical results and field measurements demonstrated that the ensemble approach consistently outperformed the standalone ConvLSTM models, particularly in long-term multi-step prediction, exhibiting reduced error propagation and improved generalization. These findings underscore the potential of multi-resolution ensemble strategies that jointly exploit diverse temporal input scales to enhance predictive stability and accuracy in AI-driven geotechnical forecasting.

Keywords: Convolutional long short-term memory, Retaining structure, Stacking ensemble, Time series prediction

1. Introduction

The deformation of retaining structures due to excavation induces settlement in adjacent areas and significantly affects structural stability, necessitating rigorous monitoring and management during construction (da Silva *et al.* 2017; Zeng *et al.* 2021). Although numerical (Lim *et al.* 2023) and back analysis (Xu and Jin, 2024) methods are commonly employed to predict and manage the deformation of these structures, accurately predicting deformation remains difficult due to inherent geotechnical uncertainties (Djadouni *et al.* 2021), and the process often requires considerable time and effort. As an alternative, many studies have used Artificial Intelligence (AI) to predict the behavior of retaining walls. Considering that the behavior of retaining structures evolves over time, specialized algorithms such as Recurrent Neural Networks (RNN), Long-Short Term Memory (LSTM), and Convolutional Long-Short Term Memory (ConvLSTM) have been employed (Das *et al.* 2023; Hochreiter and Schmidhuber 1997). For instance, Tao *et al.* (2024) proposed a sequence-to-sequence ConvLSTM network to predict spatiotemporal wall deflections induced by deep excavations. Liu *et al.* (2023) developed a prediction model that combines empirical mode decomposition (EMD) and RNN to physically predict the deformation of retaining structures in ultra-deep foundation pits, showing improved predictive accuracy over traditional empirical and numerical methods. Wang *et al.* (2024) introduced a deep learning

framework based on spatiotemporal feature fusion to enhance excavation stability predictions, which was validated through extensive case studies and demonstrated superior performance and generalizability compared to existing models. Zhao *et al.* (2021) proposed a Convolutional Neural Network (CNN)-based prediction method for concrete diaphragm wall deflections, achieving enhanced accuracy and efficiency relative to other RNN algorithms, and validating it through a deep excavation project in Suzhou, China. Samadi *et al.* (2024) compared diverse machine learning algorithms for predicting sidewall displacement in underground caverns and confirmed that the Backpropagation Neural Network (BPNN) provided the highest prediction accuracy. Seo and Chung (2022) suggested a methodology to predict the lateral displacement of braced walls at each excavation stage, which employed a convolutional neural network in conjunction with an LSTM network, demonstrated its applicability for safety management and risk mitigation in construction.

Although previous studies primarily focused on retaining structures, many researchers have explored the time-series behavior of various civil engineering systems and have demonstrated the superior performance of AI techniques. For instance, Mahmoodzadeh *et al.* (2022) developed and optimized an LSTM-based deep neural network model using 550 tunnel monitoring datasets to accurately predict tunnel wall convergence, outperforming traditional machine learning models such as Gaussian regression, support vector regression, K-nearest neighbors, and decision tree. Yu *et al.*

^a Doctoral Student

* Corresponding author, Professor
E-mail: geotech@hongik.ac.kr

(2021) compared the performance of XGBoost, LSTM, and an Autoregressive Integrated Moving Average (ARIMA) model for time-series prediction in coastal bridge engineering, concluding that while all models could predict data trends over time, LSTM exhibited superior accuracy, particularly with improved data preprocessing and multi-step predictions. Ma *et al.* (2021) introduced a novel deep learning approach employing a temporal graph convolutional network to predict slope deformation, taking into account spatial correlations between monitoring points, thereby providing a more comprehensive early warning system for slope failure compared to traditional models. Mostafaei and Soleimani (2025) integrates Particle Swarm Optimization and neural network to develop a hybrid model that accurately predicts embankment dam displacement under dynamic loading using real-case data, demonstrating significantly improved performance over soft computing methods, making it a strong reference for neural network-based predictive modeling in geotechnical engineering. Yang *et al.* (2019) presented a dynamic model utilizing time series analysis and LSTM network to predict landslide displacement in the Three Gorges Reservoir Area, demonstrating that the LSTM network outperformed static models by accurately capturing complex, nonlinear, and stepwise displacement patterns influenced by seasonal rainfall and reservoir water level fluctuations. Li *et al.* (2024) proposed a decomposition, reconstruction, and optimization method using EMD and an optimized generalized RNN algorithm for predicting tunnel settlement deformation, demonstrating significantly enhanced accuracy and reliability over traditional models when applied to shallow tunnel data. While these studies have successfully applied deep learning techniques to geotechnical engineering problems, most existing research focuses on single-step or short-term forecasts, which limits their effectiveness for long-term displacement forecasting.

In multi-step time series forecasting, two primary strategies are commonly employed: recursive (iterative) and direct method. The recursive method predicts one step ahead and recursively uses its own predictions as inputs for future steps (Yunpeng *et al.* 2017). While it is simple and flexible, this approach often suffers from error accumulation over extended prediction horizons. In contrast, the direct method predicts each fixed length of steps independently, either with separate models or a single multi-output model. This avoids the problem of error propagation but may struggle to capture temporal dependencies between prediction steps.

Su *et al.* (2025) enhanced multi-step prediction accuracy for dam displacement by incorporating a Chrono-initializer mechanism into an LSTM-based sequence-to-sequence model. However, this approach does not capture spatial correlations, exhibits performance sensitivity to the length of the training sequence, lacks flexibility in output sequence length, and tends to respond insensitively to recent input data. Dietze *et al.* (2018) proposed an iterative near-term forecasting system for ecological applications. While effective in short-term prediction, the approach incurs high computational costs due to frequent model updates and primarily focuses on short-range temporal patterns. Yang *et al.* (2024) introduced a deep learning framework leveraging

an Adams-Bashforth-based time integration scheme to account for changes across multiple future time steps. Nevertheless, their method tends to rely heavily on the distribution of the training data, limiting its ability to adapt to previously unseen patterns.

To overcome these limitations, this study suggests multi-resolution ConvLSTM ensemble framework designed to refine and enhance the multi-step accuracy in forecasting wall behavior during staged excavation. Fig. 1 illustrates the internal architecture of the ConvLSTM network. Originally developed for predicting precipitation (Shi *et al.* 2015), the ConvLSTM network processes both spatial and temporal dynamics, making it applicable across domains such as video analysis (Wang *et al.* 2017), meteorological forecasting (Zheng *et al.* 2023), and dynamic image processing (Yakkundi and Subha 2020). Leveraging these capabilities, this study employs the ConvLSTM network to predict retaining structure deformations during staged excavation. The ConvLSTM models trained on varying temporal resolutions capture multi-scale temporal patterns, and their outputs are aggregated by a fully connected deep neural network serving as a meta-learner, resulting in a hierarchical ensemble architecture that improves the robustness and reliability of long-term forecasts. The effectiveness of the proposed approach is rigorously validated using a comprehensive dataset composed of synthetic data generated via PLAXIS2D simulations and field measurements collected from two real-world excavation projects.

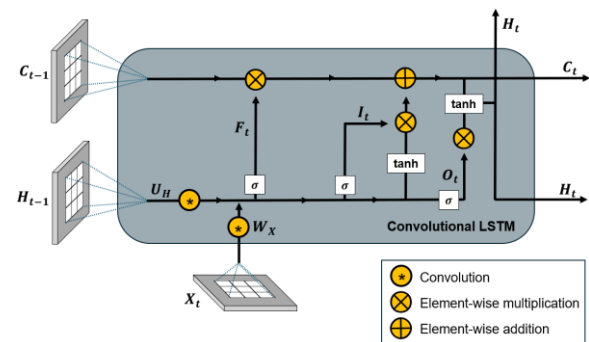


Fig. 1 Conventional ConvLSTM network

2. Methodology

2.1 Proposed framework

2.1.1 Overview

Fig. 2 presents an overview of multi-resolution ConvLSTM ensemble framework designed to refine and enhance the multi-step accuracy in forecasting wall behavior during staged excavation. The framework consists of three main stages: (1) data generation and preprocessing, (2) ConvLSTM-based multi-step prediction, and (3) stacking ensemble learning for prediction refinement.

A time-series deformation database is generated through numerical simulations using PLAXIS2D, capturing staged excavation-induced lateral displacements under varying soil conditions. The database comprises 2,000 excavation

simulations, each represented as a sequential deformation profile. Multiple ConvLSTM models are trained using different input resolution (3, 6, and 10 resolutions) to capture short- and long-term deformation dependencies. To support this, a sliding window method is applied to reformat the simulation database into sequences (e.g., using a resolution of 3 yields 66,000 sequences). A recursive multi-step forecasting strategy is employed, where single-step

predictions are iteratively used as inputs for future predictions. The outputs of different ConvLSTM models are aggregated using a stacking ensemble approach that applies deep learning (DL) based meta-learning technique. This framework enables the model to leverage diverse temporal dependencies captured by different input resolutions.

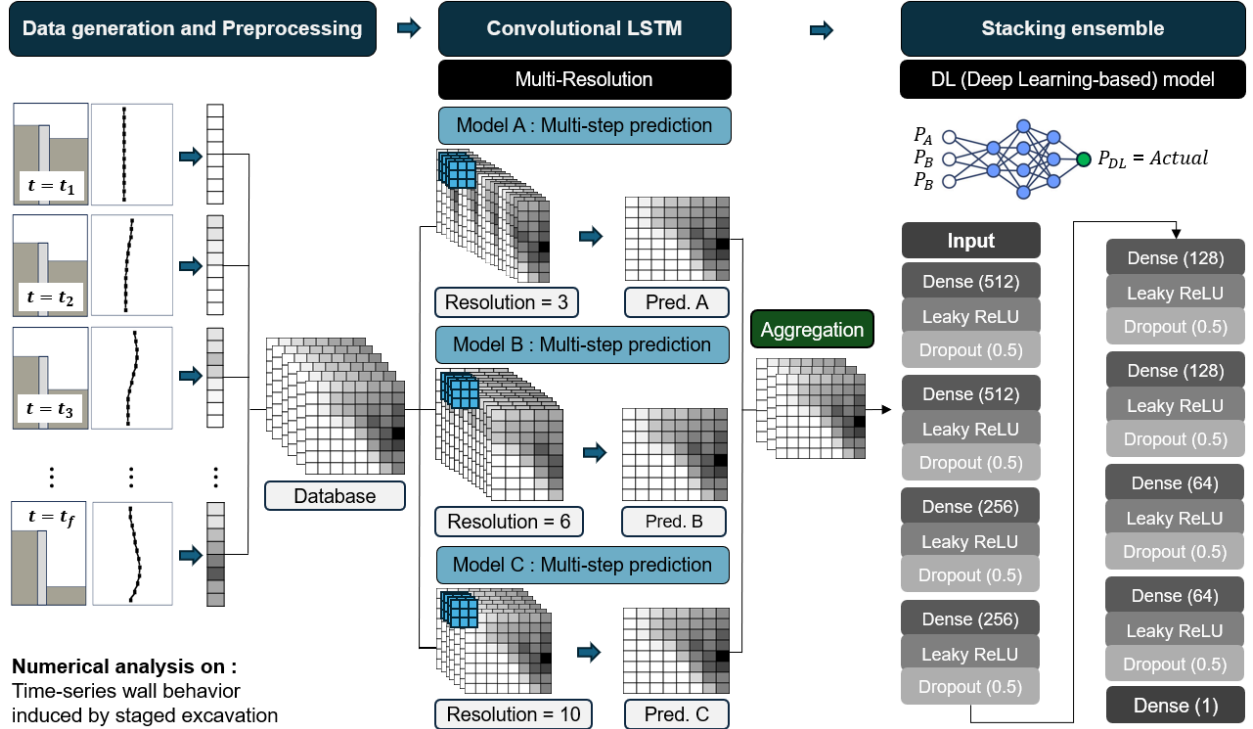


Fig. 2 Overview of the proposed multi-resolution ConvLSTM ensemble framework

2.1.2 Recursive forecasting

Multi-step forecasting is a critical aspect of time-series prediction (Wang *et al.* 2023), particularly in geotechnical applications where deformation patterns evolve progressively over time. To perform multi-step prediction, recursive forecasting, which is one of the fundamental strategies for long-term prediction, was employed (Taib and Bontempi, 2011). In recursive forecasting, the ConvLSTM model is initially trained for single-step forecasting, where it learns to predict next step based on a fixed-length sequence of past observations (i.e., resolution). Once trained, the model extends its forecasting capability by using its own predictions as inputs for future predictions. This process is repeated iteratively, allowing the model to generate multi-step forecasts beyond the original training window. Fig. 3 demonstrates this process in two parts. On the left, the training phase is shown where overlapping sequences are extracted from the time-series deformation data. Each sequence consists of a fixed number of past observations, determined by the resolution setting. On the right, the multi-step prediction process is illustrated where the model recursively generates predictions step-by-step, using previously predicted values as new inputs. It should be noted

that each model is trained independently, and their outputs are combined with true labels to train the stacking ensemble model.

One of the key challenges in recursive multi-step forecasting is error propagation. As predictions are fed back into the model, small inaccuracies in early steps tend to amplify over time, degrading overall prediction reliability. This challenge was mitigated by employing a stacking ensemble approach (Divina *et al.* 2018). In this study, multiple ConvLSTM models are trained with different resolutions. This will be discussed in the following section.

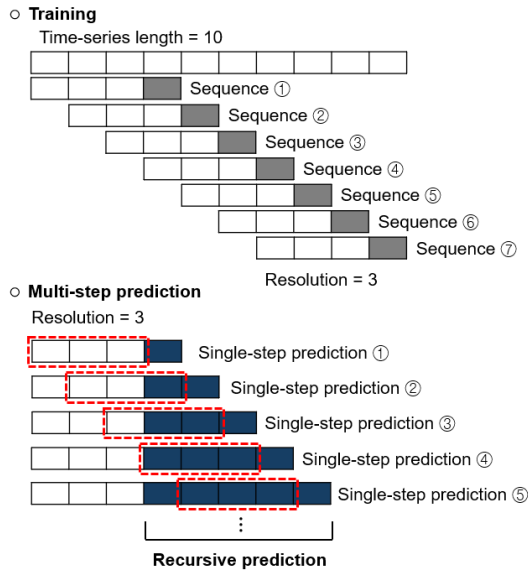


Fig. 3 Example of recursive multi-step prediction process (resolution=3)

2.1.3 Stacking ensemble

The ConvLSTM-based network used in this study is designed for multi-step prediction with a resolution of 3, 6, and 10. The architecture consists of a series of ConvLSTM layers with progressively decreasing filter sizes (128, 64, 32, and 8) to extract hierarchical spatiotemporal features from the input sequences. The models were trained using the Adam optimizer with a learning rate of 0.001, and the loss function was set to mean squared error (MSE). For each resolution configuration, the model receives input sequences of shape (None, t , 100, 1), where t represents the resolution (3, 6, or 10), 100 denotes the spatial locations, and 1 is the number of features per location. The network consists of four ConvLSTM layers with filter sizes of 128, 64, 32, and 8, each with a kernel size of 3. A dropout layer (0.5) follows each convolution block to reduce overfitting. The activation function for all ConvLSTM layers is hyperbolic tangent (Tanh) to ensure stable gradient flow. As the input propagates through the network, the output shape transitions from (t , 100, 128) in the initial ConvLSTM layer to (t , 100, 8) in the final layer. The final ConvLSTM output is flattened into a one-dimensional vector, where the output shape depends on the resolution: i.e., (None, 240) for $t=3$, (None, 480) for $t=6$, and (None, 800) for $t=10$. This representation is then processed through a fully connected dense layer with 100 units and a linear activation function, contributing 80,100 parameters to the model. The total number of trainable parameters varies with the resolution, with $t=10$ resulting in 467,332, the most complex configuration.

The multi-resolution ConvLSTM ensemble framework, as illustrated in Fig. 2, integrates multiple ConvLSTM models trained with different resolutions to improve multi-step prediction accuracy. This approach aims to construct an ensemble model, which is designed to capture the relationship between the multi-step predictions of base models and the ground truth using deep learning technique. Specifically, for the ensemble model, a fully-connected deep neural network was trained using 10-step predictions from

ConvLSTM models at each input sequence and the corresponding numerical simulation results. The model required training to be a larger number of parameters due to its multi-layer structure, increasing computational complexity but potentially capturing more intricate dependencies in the data. The network architecture consists of nine sequential fully connected (dense) layers with a decreasing number of units: two layers with 512 units, two with 256 units, two with 128 units, and two with 64 units, followed by a final output layer with a single unit. Each dense layer was followed by a dropout layer with a rate of 0.5 to prevent overfitting. Leaky ReLU activation was applied to all layers, except for the output layer, to promote stable gradient propagation and mitigate the vanishing gradient problem during training. The model was optimized using the Adam optimizer with a learning rate of 0.001, and MSE was used as the loss function.

2.2 Data generation and preprocessing

2.2.1 Numerical simulations

Fig. 4 presents the numerical models developed in PLAXIS2D to simulate the lateral displacement behavior of a retaining wall subjected to staged excavation. The finite element models were designed to replicate excavation-induced deformation under realistic geotechnical conditions, incorporating a multi-layered soil profile (five layers), a retaining wall with struts, and staged excavation sequences. By stochastically varying geotechnical parameters and utilizing a range of wall and strut stiffness, a diverse set of time-series wall behavior data was obtained for model training. This will be discussed later.

The subsurface consists of five distinct layers, with a bedrock layer at the bottom underlying four soil layers. From the top, the thicknesses of these layers are 2, 4, 9, 9 and 16 m, respectively. Two excavation depths (Z_f) were considered: 14 m (Case A) and 20 m (Case B), with corresponding retaining wall length (L_w) of 18 and 26 m, respectively. It should be noted that the distinction between Case A and B is based on whether the wall tip is constrained. In Case B, the wall tip is embedded in the bedrock and thus constrained, whereas in Case A, it is not. The constraint condition of the wall tip significantly influences the time-series behavior of the wall during staged excavation, and by considering this condition differently, various behavioral responses can be obtained.

The retaining wall was modeled as a linear elastic material, and lateral support was provided by H-beam struts. The struts were installed at 3 m intervals along the depth of excavation, except for the first installation, which was placed 1 m below the ground surface in both cases. The excavation process was simulated in incremental phases, with soil layer being sequentially removed to replicate real-world excavation practices. The models assumed a plane strain condition, with sufficient lateral (80 m) and bottom (at least 14 m from wall end) boundary extent to prevent boundary effects from influencing wall deformations. The material properties of each layer and structural components are detailed in the following section.

2.2.2 Staged excavation

The staged excavation process was simulated using 0.5 m incremental excavation steps, replicating real-world construction practices and the sequential activation of lateral support system (strut). This methodology ensured that excavation-induced stress redistribution and wall deformations were realistically captured. The detailed excavation sequences for Case A (final depth of 14 m) and Case B (final depth of 20 m) are presented in Table 1.

As previously described, the first strut was installed at a

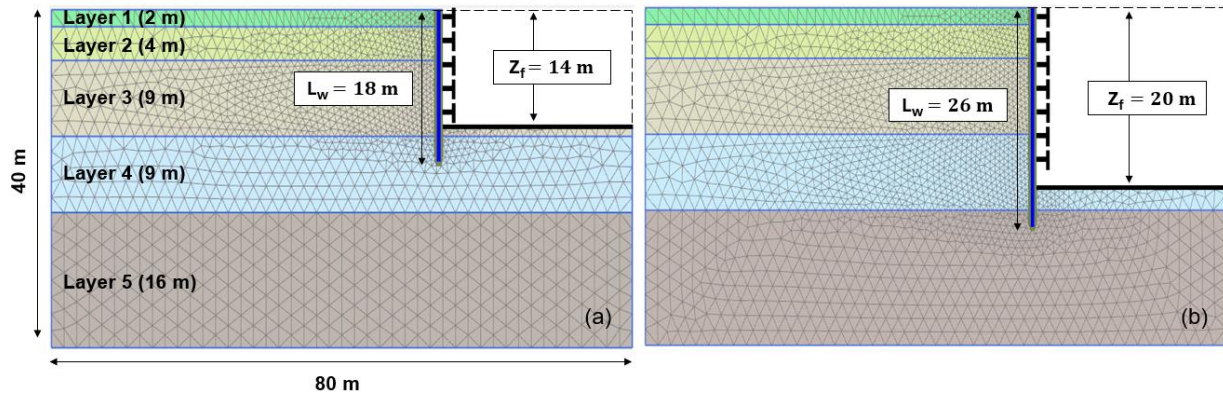


Fig. 4 Numerical models of retaining walls for training with excavation depths of: (a) 14 m (Case A) and 20 m (Case B)

Table 1 Excavation depth of strut installation for two case studies

Phase No.	Case	Excavation depth (m)	Installation
1	A B	0.0	Retaining wall
4	A B	1.5	1 st strut at 1.0 m
10	A B	4.5	2 nd strut at 4.0 m
16	A B	7.5	3 rd strut at 7.0 m
22	A B	10.5	4 th strut at 10.0 m
28	A B	13.5	5 th strut at 13.0 m
29	A	14.0 (final depth for Case A)	N/A
34	B	16.5	6 th strut at 16.0 m
40	B	19.5	7 th strut at 19.0 m
41	B	20.0 (final depth for Case B)	N/A

2.2.3 Input material parameters

The geotechnical properties of the subsurface materials were assigned based on five soil layers, consisting of four soil layers using the Hardening Soil model and one bedrock layer modeled by the Mohr-Coulomb model. The Hardening soil model was chosen for its ability to capture stress-dependent stiffness, strain-hardening behavior, and stress path effects (Teo and Wong, 2012), while Mohr-Coulomb model was applied to the bedrock, assuming a linear elastic-perfectly plastic response appropriate for stiff materials under relatively low normal stress conditions (Zhao, 2000).

To ensure the generalizability and robustness of the predictive framework, a stochastic parameter assignment approach was employed, incorporating normally distributed random sampling for key geotechnical properties.

depth of 1.0 m, with subsequent struts placed at 3.0 m intervals to maintain structural stability during excavation. The analysis assumed that no additional jacking forces were applied during strut installation, reflecting conventional field conditions. In both cases, the retaining wall was installed in the first phase before any excavation commenced. Excavation for Case A proceeded through 29 sequential phases until reaching a final depth of 14.0 m, while Case B followed 41 phases to a final depth of 20.0 m, with the same staged strut installation.

Specifically, the total unit weight (γt), internal friction angle (ϕ'), cohesion (c'), elastic modulus (E_{ref}) were assigned as random variables following a normal distribution. The mean and standard deviation of each parameter were predefined based on empirical data (Ameratunga *et al.* 2016), as summarized in Table 2. This approach introduces natural variability into the numerical database, allowing the predictive model to learn a broader range of soil behavior patterns, which is critical for improving generalization across different site conditions. Examples of normally distributed properties for Layer 1 are shown in Fig. 5. The additional elastic modulus components, E_{oed}^{ref} and E_{ur}^{ref} , in the Hardening Soil model were assigned based on predefined correlations: $E_{oed}^{ref} = E_{50}^{ref}$ and $E_{ur}^{ref} = 3 \cdot E_{50}^{ref}$, respectively. Fixed initial void ratios were used for all layers.

The structural components in the numerical model, including the retaining wall and struts, were assigned fixed material properties, unlike the soil layers where normally distributed parameters were used. However, similar to the randomized selection of soil properties, the input parameters for the retaining wall and struts were randomly selected from a predefined dataset. This ensured that different wall thickness and strut cross-sectional areas were considered in the simulations, allowing the model to learn from diverse structural conditions. The input parameters for the retaining wall and struts are summarized in Table 3 and 4.

For the retaining wall, 6 representative flexural stiffness (EI) values were defined. Wall thickness was the critical variable as EI directly dependent on thickness, influencing the wall deformation response. The flexural stiffness used in this study ranges from 100 to 1,200 MN·m²/m with corresponding wall thickness of 0.35 and 1.20 m. For the strut, a total of 6 representative axial stiffness values were

selected based on the specifications of H-beams commonly used in Korea (Korean Agency for Technology and Standards, 2021). The axial stiffness values ranged from 670 to 2,194 MN, reflecting the structural diversity in support system.

Table 2 Soil input parameters and constitutive models for each layer

Layer	Constitutive model	Input parameters	Mean value	Standard deviation
1	Hardening Soil	γ_t (kN/m ³)	18.0	2.0
		c' (kPa)	1.8	0.5
		ϕ' (°)	28.0	2.5
		E_{50}^{ref} (kPa)	15,000	3,000
		e_{init}	0.6	N/A
2	Hardening Soil	γ_t (kN/m ³)	19.0	2.0
		c' (kPa)	5.0	1.5
		ϕ' (°)	28.0	3.0
		E_{50}^{ref} (kPa)	30,000	6,000
		e_{init}	0.5	N/A
3	Hardening Soil	γ_t (kN/m ³)	20.0	2.0
		c' (kPa)	20.0	5.0
		ϕ' (°)	32.0	3.0
		E_{50}^{ref} (kPa)	40,000	8,000
		e_{init}	0.4	N/A
4	Hardening Soil	γ_t (kN/m ³)	21.0	2.0
		c' (kPa)	50.0	10.0
		ϕ' (°)	32.0	3.0
		E_{50}^{ref} (kPa)	60,000	15,000
		e_{init}	0.4	N/A
5	Mohr-Coulomb	γ_t (kN/m ³)	23.0	2.0
		c' (kPa)	80.0	20.0
		ϕ' (°)	35.0	3.0
		E'_{ref} (kPa)	1,000	200
		e_{init}	0.01	N/A

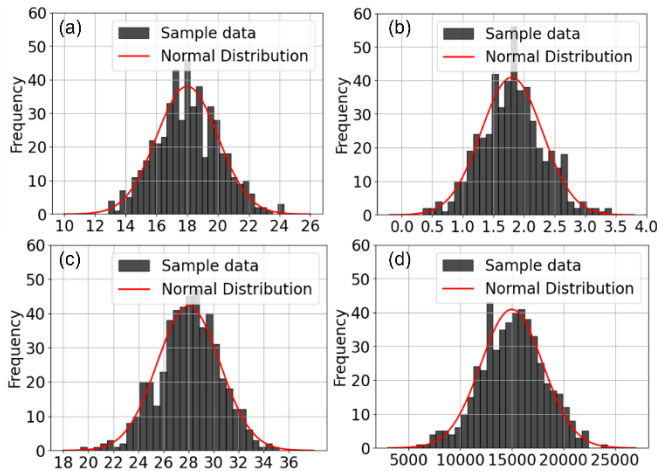


Fig. 5. Example of statistical distribution of soil input parameters (Layer 1), (a) total unit weight, (b) cohesion, (c) internal friction angle, and (d) elastic modulus

Table 3 Randomly selected input parameters for the retaining wall

Type	A	B	C	D	E	F
Flexural stiffness (MN·m ² /m)	100	200	400	600	800	1,200
Thickness (m)	0.35	0.49	0.70	0.85	0.98	1.20

Table 4 Randomly selected input parameters for struts

Type	A	B	C	D	E	F
Cross-sectional area (mm ²)	3,270	4,680	5,620	7,240	8,820	10,700
Axial stiffness (MN)	670	959	1,152	1,484	1,808	2,194
Elastic modulus (MPa)	200,500					

2.3 Database construction

To systematically generate a large-scale training database, the entire numerical simulation process, including model execution, stepwise data extraction, and preprocessing, was fully automated using the PLAXIS2D API and Python scripting. Lateral wall displacements were extracted from designated monitoring points spaced at 0.5 m intervals along the retaining wall, covering its entire height.

In Case A, 37 monitoring points recorded displacement data across 29 excavation phases, while in Case B, 53 monitoring points captured deformation over 41 phases. A total of 1,000 numerical simulations were conducted for each case, yielding a database of 2,000 simulations. To mitigate issues such as vanishing and exploding gradients during model training, displacement values were systematically stored in meters to maintain a numerically stable range. This unit selection is particularly advantageous given that excavation-induced wall displacements in the elastic range rarely surpass 1.0 m. By adopting meters as the standard unit, numerical conditioning is improved, facilitating more stable gradient propagation and ultimately promoting stable model convergence and reliability.

To ensure that the predictive model could handle walls of different lengths while maintaining a consistent input format, the extracted displacement profiles were normalized to a fixed spatial resolution. The raw displacement values from numerical simulations were spline-interpolated to 100 evenly spaced points along the wall length, standardizing the database and allowing for a uniform input structure regardless of excavation depth. This preprocessing step ensured that all simulations contributed the same number of spatial features to the training database, preventing discrepancies due to the wall length variations.

Following spatial normalization, the interpolated displacement profiles were structured for training. The collected data were stacked along the batch axis, effectively grouping them for unified processing. Finally, the entire database was reshaped and restructured according to the predefined resolutions. Specifically, for Case A, the resulting

data had dimensions of (1,000, 29, 100, 1), and for Case B, dimensions of (1,000, 41, 100, 1), where the first dimension represents the batch size, the second represents the time-series length (excavation phases), the third represents the interpolated wall length (100 points), and the fourth represents the number of features (displacement in this study). The database was then reformatted into (N, 3, 100, 1), (N, 6, 100, 1) and (N, 10, 100, 1) for different temporal resolutions based on sliding window method, where N denotes the number of sequence samples. For example, with a resolution of 3, a total of 66,000 sequences were generated. Then, the reformatted dataset was divided into train, validation, and test sets at a ratio of 7:2:1, resulting in 46,200 training

sequences, 13,200 validation sequences, and 6,600 test sequences, respectively.

It should be noted that each resolution corresponds to a 0.5 m change in excavation depth, thus, resolutions of 3, 6, and 10 indicate that wall deformation over excavation depths of 1.5 m, 3.0 m, and 5.0 m, were respectively used to generate predictions. Fig. 6 illustrates the time-series lateral displacement profiles of the retaining wall obtained from the numerical simulations for Case A and Case B. As excavation progresses, lateral displacements increase, with Case B exhibiting ordinarily greater overall displacement than Case A, reflecting the effect of increased excavation depth.

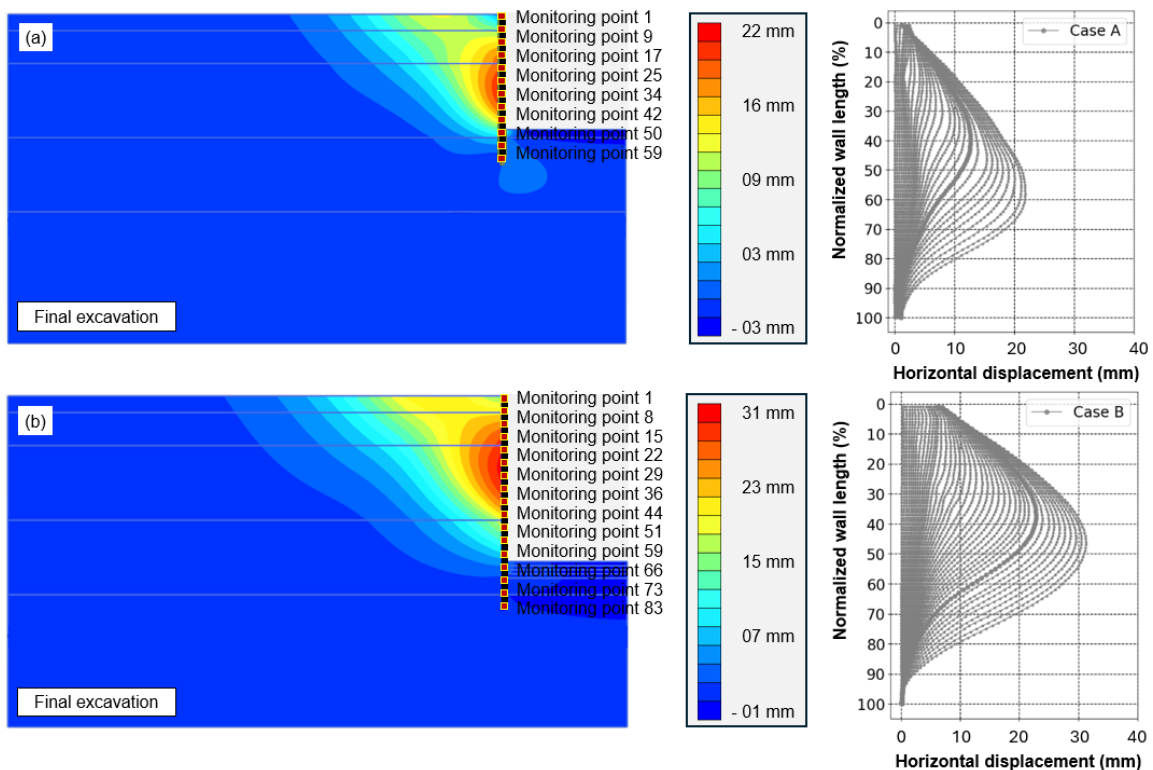


Fig. 6 Numerical simulation results and the obtained wall displacement of (a) Case A and (b) Case B

3. Results and Discussion

3.1 Multi-step prediction for numerical results

The overall multi-step prediction performance of standalone ConvLSTM models and stacking ensemble model (DL model) is presented in Fig. 7, which illustrates the trends in Mean Absolute Error (MAE), Coefficient of Determination (R^2), and Index of Agreement (IoA) (Sethy *et al.* 2025) across different prediction steps. These results were derived by averaging the MAE, R^2 , and IoA values computed for each sequence within the test set (10% of total database). The results highlight the error accumulation inherent in recursive forecasting and demonstrate the effectiveness of the stacking ensemble approach in mitigating this issue.

The standalone ConvLSTM models (A, B, and C) exhibit a clear increase in MAE as the prediction horizon extends. The error accumulation is most pronounced in Model C

(resolution = 10), followed by Model A (resolution = 3) and Model B (resolution = 6). The R^2 values (Fig. 7(d)) shows significant drop beyond 3rd prediction step for all models, with the Model C experiencing the steepest decline, and the values fall below 0 at 7th prediction step for all models, confirming that long-term predictions become increasingly unreliable due to cumulative errors. These results emphasize the limitations of using standalone models for extended multi-step prediction.

In contrast, the DL model demonstrates significant improvements over the standalone models. The DL model consistently yields lower MAE while maintaining higher R^2 and IoA values across all prediction steps. It maintains an IoA above 0.94 even at 10th prediction step, indicating its ability to stabilize long-term predictions and suppress error propagation. This observation confirms that the stacking ensemble approach significantly enhances the predictive accuracy of multi-step forecasting.

Fig. 8 presents an example of multi-step prediction using

standalone models and ensemble model for forecasting lateral wall displacements during staged excavation. For numerical simulation results, Model B is identified as the most accurate model among standalone models. Accordingly, stepwise IoA values of Model B and DL model are presented and compared, highlighting the effectiveness of the proposed framework in improving multi-step predictive accuracy.

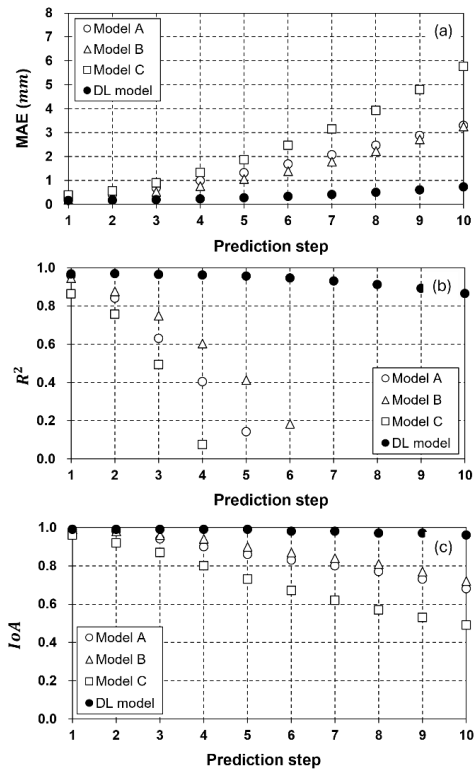


Fig. 7 Averaged multi-step prediction performance of standalone ConvLSTM and stacking ensemble models for numerical simulation results: (a) MAE, (b) R^2 , and (c) IoA

The leftmost plot represents the numerical simulation results from steps t_1 to t_{10} , which were used as input sequence to predict the subsequent seven steps from t_{11} to t_{17} . The standalone models (Model A, B, and C) employed different resolution configurations, utilizing the most recent 3, 6, and 10 steps, respectively, to generate predictions. The subsequent plots compare actual displacement profile (numerical simulation results) with predictions from four different models. As excavation progresses, the lateral displacement increases, reflecting the excavation-induced wall deformation. While all models initially exhibit high accuracy ($\text{IoA} > 0.97$), deviations from actual displacement become more pronounced for the standalone models as the prediction horizon extends, consistent with earlier findings. For short-term predictions (t_{11} - t_{13}), all models closely follow the actual displacement trend. However, error accumulations intensify in the models over longer horizons, leading to overestimation by Models A and B and underestimation by Model C. In contrast, DL model effectively integrates the predictive attributes of the standalone models, yielding more accurate multi-step forecasting. Notably, the DL model achieved the highest accuracy, maintaining IoA of 0.98 at

10th prediction step, demonstrating its reliability in predicting excavation-induced wall deformations under FEM analysis. In contrast, Model B exhibited a significantly lower IoA of 0.62 at the same step.

Fig. 9 illustrates another example of multi-step prediction, following the same forecasting process as Fig. 8 but employs a shifted input sequence (from steps t_{10} to t_{19}) to generate predictions for steps from t_{20} to t_{26} , enabling for a comparative assessment under different prediction conditions. The overall trends in model performance remain consistent with Fig. 8. The standalone models again exhibit increasing deviation over longer prediction horizons, with Model C demonstrating the highest error accumulation. Models A and B continue to overestimate displacement, while Model C tends to underestimate it in later steps. The DL model once again outperformed the standalone models, achieving the most accurate multi-step predictions, maintaining IoA of 0.98 at 10th prediction step. A similar trend is observed across other input sequences, confirming that stacking ensemble framework significantly enhances long-term prediction accuracy.

To better explain the internal decision-making process of the ensemble model, we investigated the contribution of each standalone model (Model A, B, and C) to the ensemble prediction at each forecasting step. The Shapley Additive exPlanations (SHAP) summary plots (Salih *et al.* 2025) presented in Fig. 10, visualize how the contributions of the standalone models to the final ensemble prediction evolve over the course of 10 prediction steps, based on the entire test set (approximately 6,600 sequences). Each subplot corresponds to a specific prediction step and illustrates the SHAP values associated with each standalone model's prediction, where the horizontal axis represents the contribution to the ensemble output and the color encodes the magnitude of the standalone model's prediction (i.e., feature value). These plots allow for a detailed inspection of not only how much influence each standalone model has on the ensemble decision, but also how that influence varies across the prediction horizon.

In these plots, larger absolute SHAP values indicate greater impact on the ensemble output, while the sign of the SHAP value reflects whether the base model's prediction increased or decreased the final forecast. Across all prediction steps, several consistent patterns are observed. Most notably, Model C exhibits the largest spread in SHAP values throughout all prediction steps, indicating that its predictions contribute most significantly to the ensemble model's output. Model A generally shows intermediate levels of influence, while Model B consistently displays the smallest SHAP value distribution, suggesting it plays a more limited role in the final prediction. This ordering of influence (Model C > A > B) remains stable across the forecast horizon. In addition, as the prediction step increases, the overall SHAP distributions tend to widen for all models. This broadening can be interpreted as an increase in predictive uncertainty; that is, the ensemble model becomes more sensitive to the input predictions as the temporal distance from the conditioning input grows. Interestingly, although Model B achieves the highest prediction accuracy among standalone models (refer to Fig. 7), its influence on the

ensemble prediction is consistently the lowest. Conversely, despite being the weakest individual performer, Model C contributes most heavily within the ensemble framework. This apparent discrepancy might be explained by the training mechanism of the ensemble model, which is optimized not for the accuracy of individual inputs, but rather for the

overall reduction of ensemble prediction error. In this context, the ensemble may find Model C useful not for its correctness, but for its ability to provide diverse or corrective signals that compensate for the systematic biases of other models.

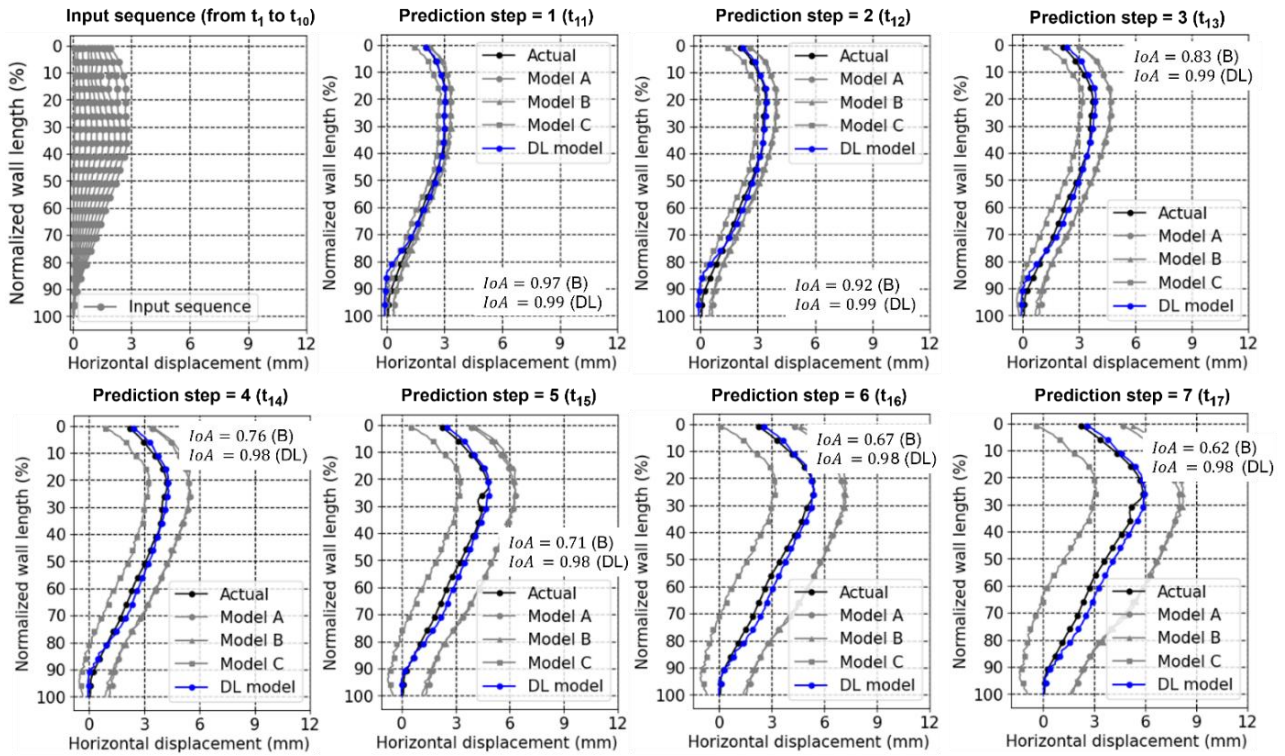


Fig. 8 Multi-step predictions of standalone ConvLSTM and ensemble models using input sequence from steps t_1 to t_{10}

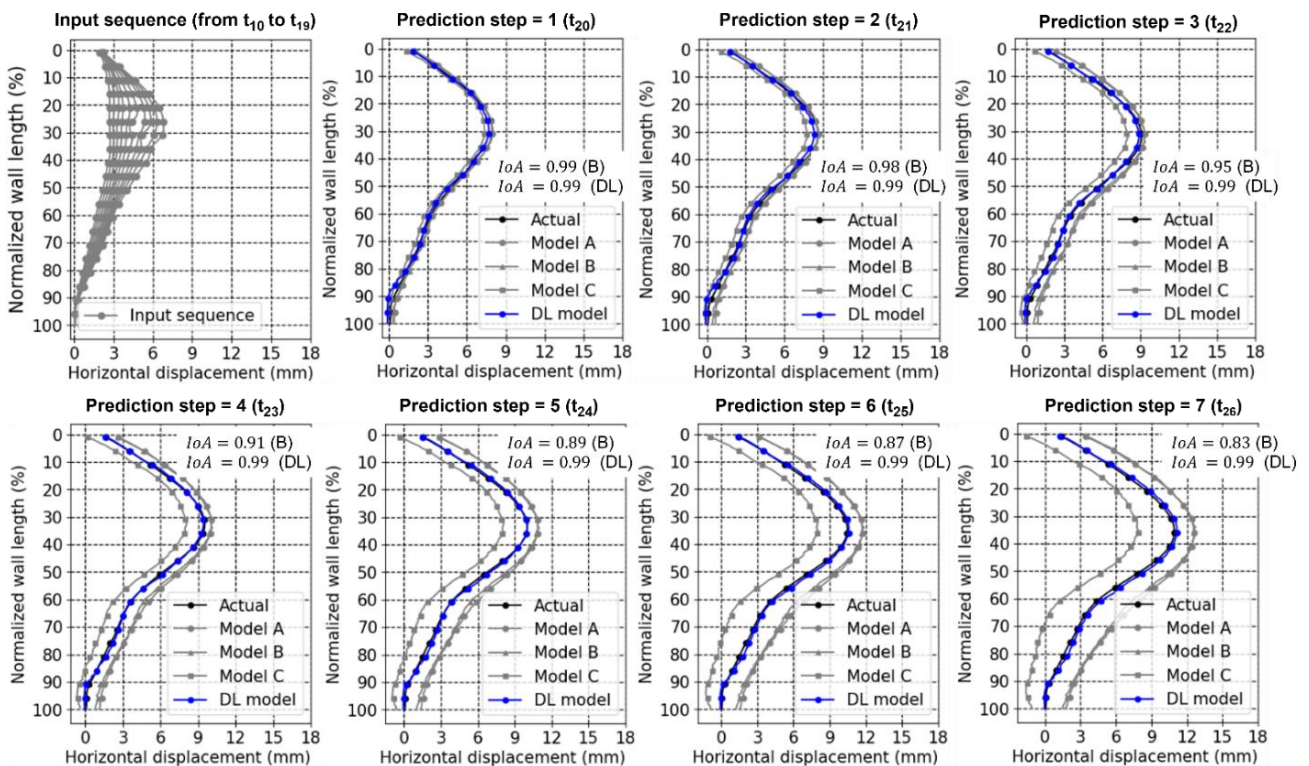


Fig. 9 Multi-step predictions of standalone ConvLSTM and ensemble models using input sequence from steps t_{10} to t_{19}

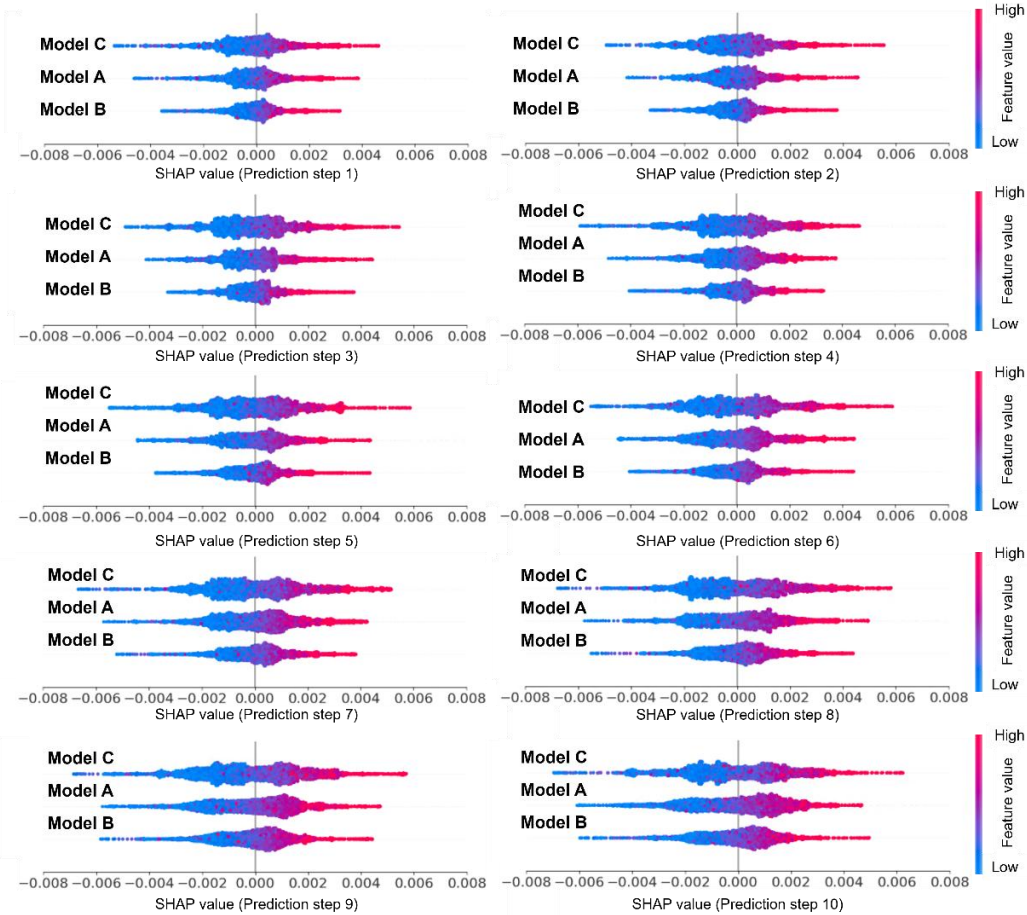


Fig. 10 SHAP value distributions for Model A, B, and C across prediction steps 1 to 10, showing their contributions to the ensemble model's predictions

3.2 Validation with field measurements

To evaluate the practical applicability of the developed framework, the multi-step predictive accuracy of standalone and ensemble models was evaluated using time-series field measurements of retaining wall displacements from two urban inland excavation sites in South Korea. Fig. 11 presents the lateral displacement profiles for Site A and B (Seo and Chung, 2023), illustrating the observed wall deformations during staged excavation.

At Site A, a total of 53 displacement measurements were recorded from June 9, 2020, to March 30, 2021, with the maximum excavation depth of 11 m and a maximum lateral displacement of 11 mm. Struts and earth anchors were used as support systems, with displacement profile (Fig. 11(a)) exhibiting localized variations, particularly in the upper half of the wall. Displacements were recorded at 43 monitoring points, spaced at 0.5 m intervals along the wall. At Site B, 35 displacement measurements were collected from June 24, 2021, to January 5, 2022, with a maximum excavation depth of 15 m and a maximum observed displacement of 7 mm. Unlike Site A, employing only struts as support systems, the displacement profile (Fig. 11(b)) follows a more uniform deformation trend, with lateral displacement progressively along the wall height. Displacement was recorded at 22 monitoring points, spaced at 0.5 m intervals along the wall.

To ensure consistency in data processing, the measurements at the monitoring points were interpolated to generate 100 evenly spaced points along the wall for further analysis. While the numerical simulation data used for training exhibited a uniformly increasing displacement trend, the field measurements in Fig. 11 display irregular and inconsistent patterns, largely due to non-uniform excavation progress and site-specific geotechnical conditions. These displacement profiles provide a real-world basis for model validation, enabling an assessment of prediction accuracy under practical excavation conditions.

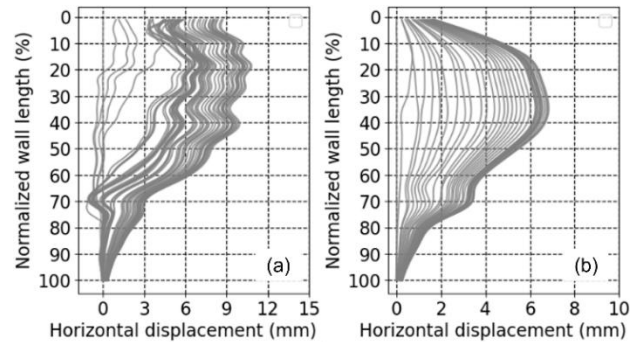


Fig. 11 Field measurements for model validation at (a) Site A and (b) Site B

3.2.1 Site A

Fig. 12 displays the overall multi-step prediction performance of all models, which was obtained by averaging MAE, R^2 , and IoA values across all sequences within the field measurement at Site A (Fig. 11(a)). The results confirm that the stacking ensemble model (DL model) significantly outperforms the standalone ConvLSTM models (Model A, B, and C), achieving lower MAE while maintaining higher R^2 and IoA values across all prediction steps. Notably, the DL model sustains an IoA of approximately 0.90 even at 10th prediction step, demonstrating its effectiveness in stabilizing long-term predictions and mitigating error propagation. These findings indicate that the stacking ensemble approach substantially enhances multi-step prediction accuracy and extends the reliable prediction horizon beyond that of standalone ConvLSTM models.

In contrast, the standalone models exhibit a clear increasing trend in MAE as the prediction horizon extends, reflecting error accumulation in recursive forecasting. Among them, Model A (resolution = 3) exhibits the highest error accumulation, followed by Model C (resolution = 10) and B (resolution = 6). While Model B shows relatively lower errors, all standalone models experience significant performance degradation over longer prediction horizons. Additionally, the IoA values (Fig. 12(d)) experience a notable decline beyond 5th prediction step for all standalone models, with Model A showing the steepest drop. By 8th prediction step, the IoA values fall below 0.8 for all standalone models, confirming that long-term predictions become unreliable due to cumulative errors. While single-step predictions ($\text{IoA} > 0.98$) remain highly accurate, these results indicate that standalone models are severely insufficient for extended multi-step forecasting.

Fig. 13 presents an example of multi-step predictions using the standalone and stacking ensemble models with field measurements at Site A. The leftmost plot represents the field measurements from steps t_{19} to t_{28} (from August 17, 2020, to September 18, 2020), which were used as input sequence to predict the subsequent seven steps from t_{29} to t_{35} (from September 22, 2020, to October 20, 2020). The following plots compare the actual displacement profiles (field measurements) with the predictions from four models, evaluating their accuracy as the prediction horizon extends. For Site A, Model B is identified as the most accurate model among standalone ConvLSTM. Accordingly, their stepwise IoA values of Model B and DL model are also presented and compared.

In the short-term predictions (t_{29} - t_{32}), all models closely track the actual displacement trend with IoA values exceeding 0.95. The DL model demonstrates particularly

robust agreement with the measured data, while the standalone models also perform well, showing only minor deviations. As the prediction horizon extends beyond t_{33} , discrepancies between predicted and actual displacement profiles become more pronounced, particularly for the standalone models. By step t_{33} , (October 13, 2020), IoA of model B declines from 0.88 to 0.78 at t_{35} (October 20, 2020), indicating severe error accumulation. In contrast, the stacking ensemble model consistently outperforms the standalone models across all prediction steps. The DL model shows superior predictive stability, with IoA remaining above 0.97 even at t_{35} . Unlike standalone models, which tend to overestimate or underestimate displacements at later steps, ensemble model closely aligns with actual field measurements. A similar trend is observed across other input sequences, confirming that stacking ensemble framework significantly enhances long-term prediction accuracy even with field measurements.

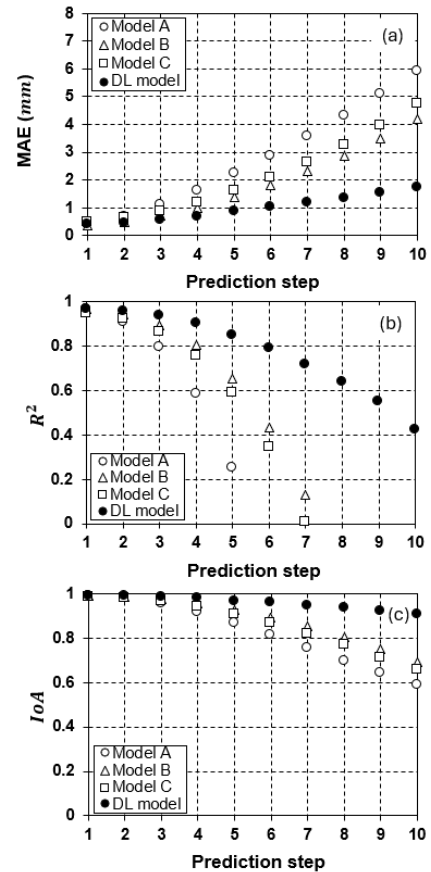


Fig. 12 Averaged multi-step prediction performance of standalone ConvLSTM and ensemble models for field measurements at Site A: (a) MAE, (b) R^2 , and (c) IoA

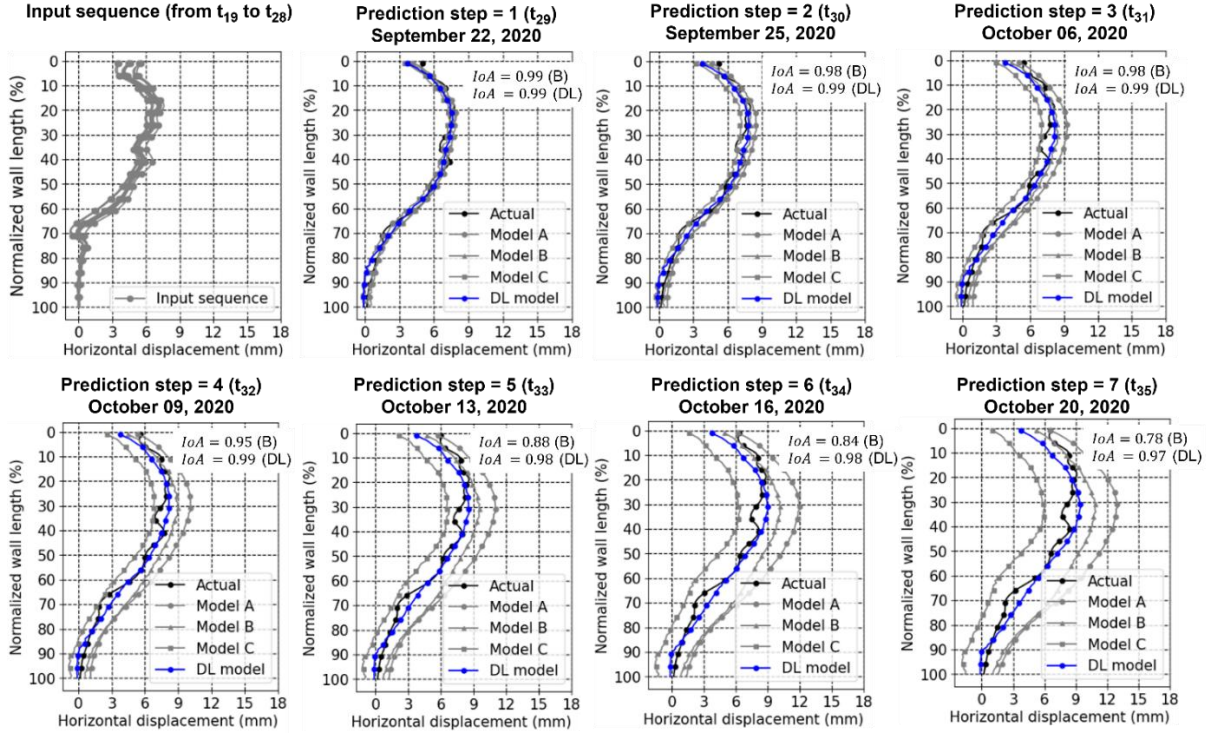


Fig. 13 Multi-step predictions of standalone ConvLSTM and ensemble models using input sequence from steps t_{19} to t_{28}

3.2.2 Site B

Fig. 14 shows the multi-step prediction performance for Site B using the measurement data in Fig. 11(b). As with Site A, standalone models accumulate errors over longer horizons, whereas the stacking ensemble model achieves higher accuracy and stability. It maintains an IoA above 0.9 up to the 10th step, indicating strong reliability in long-term predictions.

Fig. 15 presents an example of multi-step prediction at Site B, using input sequences from steps t_1 to t_{10} (from June 24, 2021, to July 26, 2021) to predict the subsequent seven steps from t_{11} to t_{17} (from July 29, 2021, to August 26, 2021). For Site B, Model C is identified as the most accurate model among standalone models. Accordingly, stepwise IoA values of Model C and DL model are also presented and compared. Similar to the prediction results for Site A, all models initially demonstrate high predictive accuracy ($\text{IoA} > 0.97$). However, as the prediction horizon extends, deviations from actual displacement become more evident in the standalone models, reinforcing earlier observations. For short-term predictions (t_{11} – t_{14}), all models align well with the actual displacement trend. However, as the prediction horizon extends, cumulative errors become more pronounced. In contrast, DL model integrates the predictive strengths of the standalone models, resulting in more reliable multi-step forecasts. Particularly, the DL model maintains an IoA above 0.96 even at 7th prediction step, demonstrating its ability to predict wall behavior accurately up to three weeks in advance. In contrast, Model C exhibits a significantly lower IoA of 0.73 at the same step, highlighting superior predictive performance of the DL ensemble model. A similar tendency was observed in other input sequences, reinforcing that the stacking ensemble

framework greatly improves long-term prediction accuracy, even when applied to field measurements.

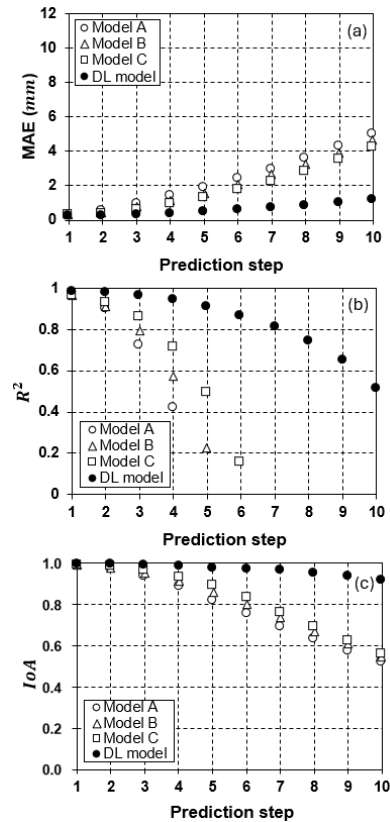


Fig. 14 Averaged multi-step prediction performance of standalone ConvLSTM and ensemble models for field measurements at Site A: (a) MAE, (b) R^2 , and (c) IoA

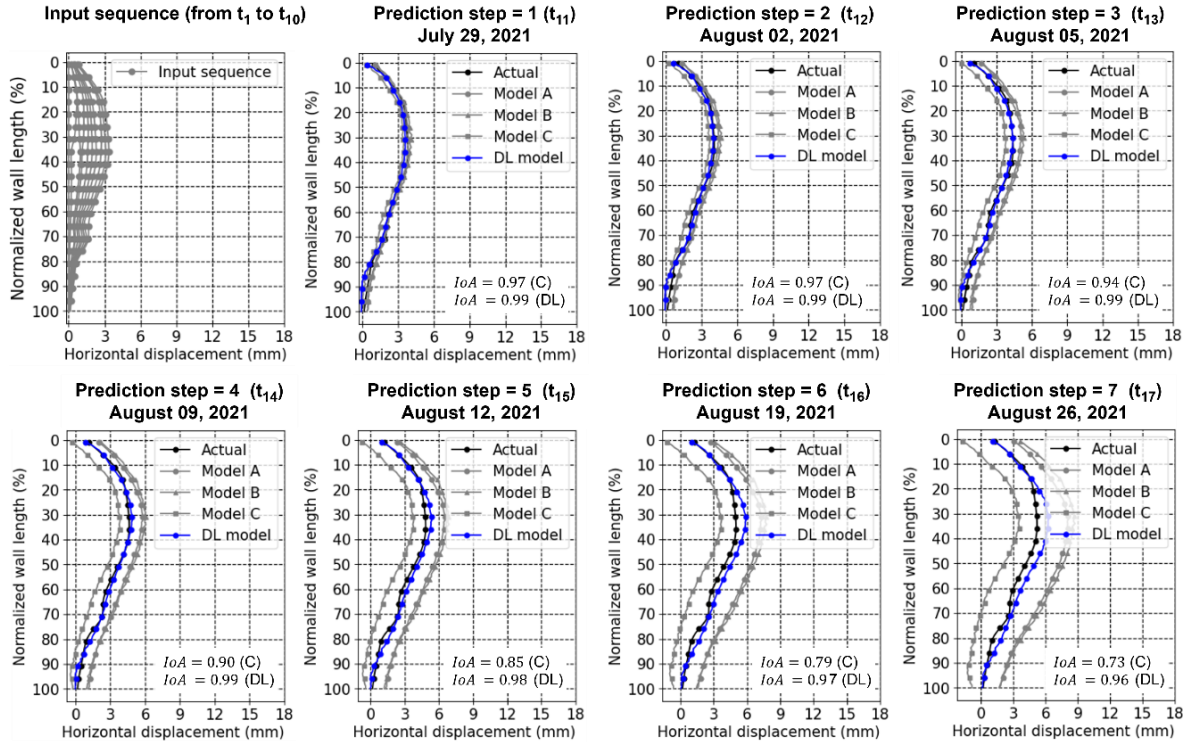


Fig. 15 Multi-step predictions of standalone ConvLSTM and ensemble models using input sequence from steps t_1 to t_{10}

3.2.3 Interpreting ensemble behavior via SHAP analysis

Fig. 16 presents the normalized contribution of the three standalone ConvLSTM models to the ensemble's prediction across all prediction steps. Contributions were calculated by averaging the absolute SHAP values for each model at each prediction step and normalizing them so that the sum across all three models equals one. In the numerical test set (approximately 6,600 sequences), as shown in the Fig. 16(a), Model C dominates early forecasts, with its contribution initially exceeding those of Model A and B, by 10th step the gap between their contributions have narrowed, yielding a more balanced influence among all three models. In the field cases (Site A in Fig. 16(b) and Site B in Fig. 16(c)), however, the relative contributions undergo a pronounced shift: Model C's lead diminishes as the prediction horizon extends, while Model A's share steadily grows, surpassing Model C by the final prediction step. These trends indicate that under irregular field conditions, the ensemble increasingly relies on the shortest-window model (Model A) as predictions advance.

To better understand the mechanisms behind these SHAP-based contribution shifts, Fig. 17 compares single-step predictions from Models A and C on Site B using the input sequence from t_1 to t_{10} . Both models were trained exclusively on numerical simulation data, where wall deformations increase smoothly and monotonically; accordingly, they should predict a displacement exceeding the final input value. Model A's output (Fig. 17(b)) conforms to this expectation, exhibiting a clear increasing trend beyond t_{10} . In contrast, Model C (Fig. 17(c)) often produces predictions that stagnate or even decrease compared to the last input.

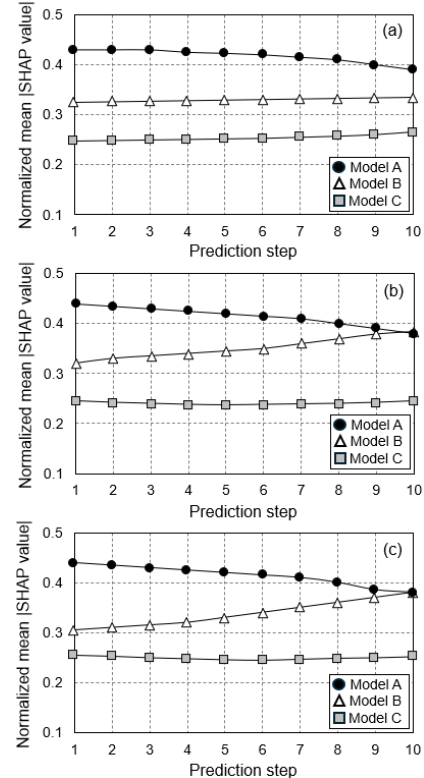


Fig. 16 Stepwise relative contributions of standalone models to ensemble prediction for (a) numerical test set, (b) Site A field measurement, and (c) Site B field measurement

We attribute this divergence to two key factors. First, the numerical simulations used for training lack the irregular,

nonlinear fluctuations present in field measurements, so models tuned on those data struggle to adapt to real-world variability. Second, each model's input window length governs its responsiveness: Model A, with resolution of 3, quickly adapts to recent changes, while Model C, with resolution of 10, smooths over sudden shifts and follows the overall trend. In standalone operation, Model C's tendency to overlook sudden deviations generates early-step errors that propagate through its recursive forecasts, degrading its long-term accuracy.

Crucially, the ensemble framework overcomes these individual shortcomings by effectively adjusting the influence of each model based on the current input. As field-driven variations intensify, the meta-learner tends to rely more on Model A, whose outputs provide sharper directional cues, and less on Model C, thereby mitigating the propagation of early-step errors. This adaptive behavior is reflected in the rising SHAP values for Model A shown in Fig. 16. Although the ensemble's internal weights remain fixed after training, its nonlinear structure allows the contribution of each model to vary with the input, resulting in context-dependent amplification or suppression of individual outputs. Consequently, the ensemble not only

compensates for the weaknesses of standalone models but also leverages the complementary strengths of Models A and C to deliver robust, long-term forecasts under complex field conditions.

Building on these observations, the results demonstrate the practical advantage of combining standalone models with different temporal resolutions in a single ensemble. Higher-resolution model (i.e., resolution of 3) delivers heightened sensitivity to the most recent excavation stages, enabling the ensemble to respond quickly to abrupt, site-specific changes. Conversely, lower-resolution model (i.e., resolution of 10) captures broader historical trends, stabilizing predictions and filtering out short-term noise. By integrating these complementary capabilities, the stacking ensemble harnesses multi-scale temporal information, mitigates individual model biases, and limits error accumulation over extended horizons. As a result, the ensemble consistently outperforms any single ConvLSTM model in isolation, indicating that incorporating diverse temporal resolution is an effective strategy for producing field-adaptable predictions of retaining wall behavior.

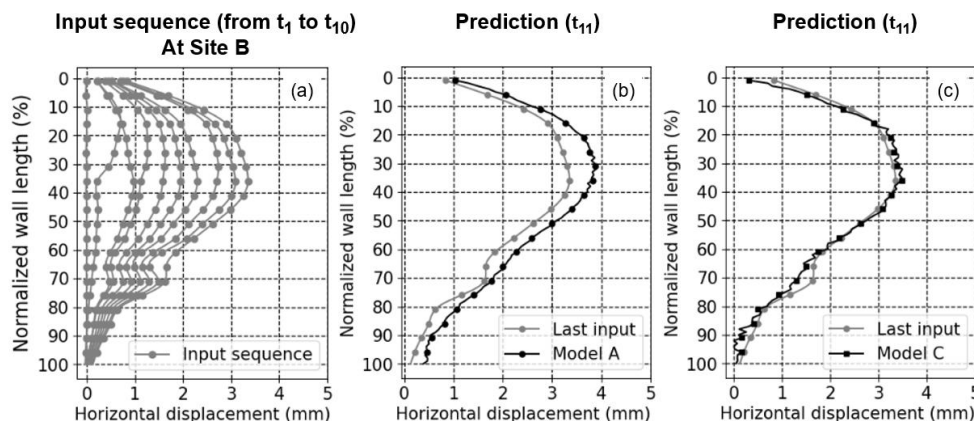


Fig. 17. Comparison of single-step predictions by standalone models A and C using field measurements at Site B: (a) input sequence, (b) prediction by Model A, and (c) prediction by Model C

4. Conclusions

In this study, we developed a multi-resolution ConvLSTM ensemble framework to improve long-horizon forecasting of retaining structure behavior during staged excavation. We generated a comprehensive numerical dataset via PLAXIS2D simulations, sampling geotechnical and structural parameters stochastically to capture site variability. Multiple ConvLSTM models, each configured with a different temporal resolution, were integrated using a deep learning-based stacking ensemble approach. The resulting framework was evaluated on both synthetic simulation results and real-world field measurements. The key findings are as follows:

- The proposed framework substantially improves multi-step predictive accuracy while effectively mitigating error accumulation, resulting in a longer and more reliable prediction horizon for retaining wall

displacements across both numerical and field datasets.

- In spatio-temporal forecasting using field measurements, the deep learning ensemble model achieved an average IoA of approximately 0.90 at the 10th prediction step (equivalent to about five weeks ahead), whereas the standalone ConvLSTM models showed pronounced error accumulation, with IoA values dropping below 0.65 at the same prediction step.
- The stacking ensemble model benefited from ConvLSTM models operating at different temporal resolutions: the low-resolution model exerts the greatest influence initially, while the high-resolution model's contribution grows over time due to its responsiveness to recent changes and its ability to capture nonlinear displacement trends.
- In numerical simulations, the deep learning ensemble model consistently mitigates error propagation compared to standalone ConvLSTM models, maintaining average IoA values above 0.95 through 10th prediction step, in

contrast to average IoA values below 0.75 for standalone models at the corresponding horizon.

- Despite being trained on an idealized FEM-derived dataset, the proposed framework effectively captures nonlinear deformation patterns in real-world conditions, suggesting a promising level of generalization across site-specific geotechnical variability.

Importantly, the integration of ConvLSTM models operating at different temporal resolutions within a stacking ensemble has shown to be a critical factor in enhancing predictive stability and accuracy over long horizons. This multi-resolution strategy allows the framework to dynamically balance long-term contextual information with short-term responsiveness, effectively compensating error accumulation over extended prediction horizon. These findings underscore the potential of multi-resolution ensemble systems in complex geotechnical forecasting. While these results are promising, further validation on additional excavation sites and integration of direct in situ sensor data will be essential to fully establish the models' robustness under diverse field conditions.

Declaration of Competing Interest

The authors declare that they have no known competing financial interests or personal relationships that could have appeared to influence the work reported in this paper.

Acknowledgments

This work was supported by the National Research Foundation of Korea (NRF) grant funded by the Korea government (MSIT) (No. 2023R1A2C1007635).

References

- Ameratunga, J., Sivakugan, N. and Das, B.M. (2016), Correlations of Soil and Rock Properties in Geotechnical Engineering, Springer, New Delhi, India
- da Silva, A.P., Festugato, L. and Masuero, J.R. (2017), "A new methodology to assess the structural safety of anchored retaining walls", *Thin-Walled Struct.*, **117**, 343–355. <https://doi.org/10.1016/j.tws.2017.04.022>
- Das, S., Tariq, A., Santos, T., Kantareddy, S.S. and Banerjee, I. (2023), "Recurrent neural networks (RNNs): architectures, training tricks, and introduction to influential research", *Mach. Learn. Brain Disord.*, **197**, 117-138. https://doi.org/10.1007/978-1-0716-3195-9_4
- Djadouni, H., Trouzine, H., Gomes Correia, A. and Miranda, T.F. da S. (2019), "2D numerical analysis of a cantilever retaining wall backfilled with sand–tire chips mixtures", *Eur. J. Environ. Civ. Eng.*, **25**(6), 1119–1135. <https://doi.org/10.1080/19648189.2019.1570870>
- Dietze, M.C., Fox, A., Beck-Johnson, L.M., Betancourt, J.L., Hooten, M.B., Jarnevich, C.S., et al. (2018), "Iterative near-term ecological forecasting: needs, opportunities, and challenges", *Proc. Natl. Acad. Sci.*, **115**(7), 1424–1432. <https://doi.org/10.1073/pnas.1710231115>
- Divina, F., Gilson, A., Gómez-Vela, F., García, T.M. and Torres, J.F. (2018), "Stacking ensemble learning for short-term electricity consumption forecasting", *Energies*, **11**(4), 949. <https://doi.org/10.3390/en11040949>
- Hochreiter, S. and Schmidhuber, J. (1997), "Long short-term memory", *Neural Comput.*, **9**(8), 1735–1780. <https://doi.org/10.1162/neco.1997.9.8.1735>
- KS D 3502 (2021), Dimensions, mass and permissible variations of hot rolled steel sections, Korean Agency for Technology and Standards; Republic of Korea
- Li, T., Shu, J. and Chang, D. (2024), "Time-series prediction of settlement deformation in shallow buried tunnels based on EMD-SSA-GRNN model", *Sci. Rep.*, **14**(1), 324. <https://doi.org/10.1038/s41598-024-51165-w>
- Lim, H., Park, J., Kim, J. and Ko, J. (2023), "Numerical study on stability and deformation of retaining wall according to groundwater drawdown". *Geomech. and Eng.*, **33**(2), 195-202. <https://doi.org/10.12989/gae.2023.33.2.195>
- Liu, Z., Liu, F., Wang, Y., Zhang, Y., Sun, Z. and Zhang, M. (2023), "Prediction of retaining structure deformation of ultra-deep foundation pit by empirical mode decomposition with recurrent neural networks", *Environ. Earth Sci.*, **82**, 553. <https://doi.org/10.1007/s12665-023-11214-5>
- Ma, Z., Mei, G., Prezioso, E., Zhang, Z. and Xu, N. (2021), "A deep learning approach using graph convolutional networks for slope deformation prediction based on time-series displacement data", *Neural Comput. Appl.*, **33**(5), 14441–14457. <https://doi.org/10.1007/s00521-021-06084-6>
- Mahmoodzadeh, A., Taghizadeh, M., Mohammed, A. H., Ibrahim, H. H., Samadi, H., Mohammadi, M., and Rashidi, S. (2022), "Tunnel wall convergence prediction using optimized LSTM deep neural network", *Geomech. and Eng.*, **31**(6), 545-556. <https://doi.org/10.12989/gae.2022.31.6.545>
- Mostafaei, Y. and Soleimani Kutanaei, S. (2025), "Modeling and prediction of embankment dam displacement under earthquake loading using artificial neural networks and swarm optimization algorithm", *Int. J. Geo-Eng.*, **16**(1), 8. <https://doi.org/10.1186/s40703-025-00235-7>
- Salih, A.M., Raisi-Estabragh, Z., Galazzo, I.B., Radeva, P., Petersen, S.E., Lekadir, K. and Menegaz, G. (2025), "A perspective on explainable artificial intelligence methods: SHAP and LIME", *Adv. Intell. Syst.* **7**(1), 2400304. <https://doi.org/10.1002/aisy.202400304>
- Samadi, H., Alanazi, A., Muhodir, S. H., Alsubai, S., Alqahtani, A., and Marzougui, M. (2024), "In-depth exploration of machine learning algorithms for predicting sidewall displacement in underground caverns", *Geomech. and Eng.*, **37**(4), 307-321. <https://doi.org/10.12989/gae.2024.37.4.307>
- Seo, S. and Chung, M. (2022), "Evaluation of applicability of 1D-CNN and LSTM to predict horizontal displacement of retaining wall according to excavation work", *Int. J. Adv. Comput. Sci. Appl.*, **13**(2), 148–156. <https://dx.doi.org/10.14569/IJACSA.2022.0130210>
- Seo, S. and Chung, M. (2023), "Development of an ensemble prediction model for lateral deformation of retaining wall under construction", *J. Korean Geotech. Soc.*, **39**(4), 5–17. <https://doi.org/10.7843/kgs.2023.39.4.5>
- Sethy, B.P., Prajapati, U.K.N., Maharana, D., Lakkimsetty, N.R. and Maurya, S. (2025), "Artificial intelligence models for predicting unconfined compressive strength of mixed soil types: focusing on clay and sand", *Asian J. Civ. Eng.*, 1–18. <https://doi.org/10.1007/s42107-025-01285-z>
- Shi, X., Chen, Z., Wang, H., Yeung, D.Y., Wong, W.K. and Woo, W.C. (2015), "Convolutional LSTM network: a machine learning approach for precipitation nowcasting", *Adv. Neural Inf. Process. Syst.*, **28**, 802–810. <https://doi.org/10.48550/arXiv.1506.04214>
- Su, Y., Fu, J., Lin, C., Lai, X., Zheng, Z., Lin, Y. and He, Q. (2025), "A novel deep learning multi-step prediction model for dam displacement using Chrono-initialized LSTM and sequence-to-sequence framework", *Expert Syst. Appl.*, **271**, 126624. <https://doi.org/10.1016/j.eswa.2025.126624>

- <https://doi.org/10.1016/j.eswa.2025.126624>
- Tao, Y., Zeng, S., Sun, H., Cai, Y., Zhang, J. and Pan, X. (2024), “A spatiotemporal deep learning method for excavation-induced wall deflections”, *J. Rock Mech. Geotech. Eng.*, **16**(8), 3327–3338. <https://doi.org/10.1016/j.jrmge.2023.09.034>
- Taieb, S.B. and Bontempi, G. (2011), Recursive Multi-step Time Series Forecasting by Perturbing Data, *Proceedings of the 2011 IEEE 11th International Conference on Data Mining (ICDM)*, IEEE, Vancouver, Canada, December
- Teo, P.L. and Wong, K.S. (2012), “Application of the Hardening Soil model in deep excavation analysis”, *IES J. Part A Civ. Struct. Eng.*, **5**(3), 152–165. <https://doi.org/10.1080/19373260.2012.696445>
- Wang, K., Wu, X., Zhang, L. and Song, X. (2023), “Data-driven multi-step robust prediction of TBM attitude using a hybrid deep learning approach”, *Adv. Eng. Inform.*, **55**, 101854. <https://doi.org/10.1016/j.aei.2022.101854>
- Wang, X., Pan, Y., Chen, J. and Li, M. (2024), “A spatiotemporal feature fusion-based deep learning framework for synchronous prediction of excavation stability”, *Tunn. Undergr. Space Technol.*, **147**, 105733. <https://doi.org/10.1016/j.tust.2024.105733>
- Wang, Y., Long, M., Wang, J., Gao, Z. and Yu, P.S. (2017), “PredRNN: recurrent neural networks for predictive learning using spatiotemporal LSTMs”, *Adv. Neural Inf. Process. Syst.*, **30**, 2829–2839. <https://dl.acm.org/doi/10.5555/3294771.3294855>
- Yang, B., Yin, K., Lacasse, S. and Liu, Z. (2019), “Time series analysis and long short-term memory neural network to predict landslide displacement”, *Landslides* **16**(4), 677–694. <https://doi.org/10.1007/s10346-018-01127-x>
- Yang, S., Vinuesa, R. and Kang, N. (2024), “Long-term autoregressive prediction using lightweight AI models: Adams-Bashforth time integration with adaptive multi-step rollout”, *arXiv*, arXiv:2412.05657. <https://doi.org/10.48550/arXiv.2412.05657>
- Yakkundi, S.V. and Subha, D.P. (2020), “Convolutional LSTM: a deep learning approach for dynamic MRI reconstruction”, *Proc. Int. Conf. Trends Electron. Inform.*, 1011–1015. <https://doi.org/10.1109/ICOEI48184.2020.9142982>
- Yu, E., Wei, H., Han, Y., Hu, P. and Xu, G. (2021), “Application of time series prediction techniques for coastal bridge engineering”, *Adv. Bridge Eng.*, **2**(1), 6. <https://doi.org/10.1186/s43251-020-00025-4>
- Yunpeng, L., Di, H., Junpeng, B. and Yong, Q. (2017), “Multi-Step Ahead Time Series Forecasting for Different Data Patterns Based on LSTM Recurrent Neural Network”, *Proceedings of the 2017 14th Web Information Systems and Applications Conference (WISA)*, IEEE, Liuzhou, China, November
- Zeng, C.F., Song, W.W., Xue, X.L., Li, M.K., Bai, N. and Mei, G.X. (2021), “Construction dewatering in a metro station incorporating buttress retaining wall to limit ground settlement: insights from experimental modelling”, *Tunn. Undergr. Space Technol.*, **116**, 104124. <https://doi.org/10.1016/j.tust.2021.104124>
- Zhao, H.J., Liu, W., Shi, P.X., Du, J.T. and Chen, X.M. (2021), “Spatiotemporal deep learning approach on estimation of diaphragm wall deformation induced by excavation”, *Acta Geotech.*, **16**(11), 3631–3645. <https://doi.org/10.1007/s11440-021-01264-z>
- Zhao, J. (2000), “Applicability of Mohr–Coulomb and Hoek–Brown strength criteria to the dynamic strength of brittle rock”, *Int. J. Rock Mech. Min. Sci.*, **37**(7), 1115–1121. [https://doi.org/10.1016/S1365-1609\(00\)00049-6](https://doi.org/10.1016/S1365-1609(00)00049-6)
- Zheng, L., Lu, W. and Zhou, Q. (2023), “Weather image-based short-term dense wind speed forecast with a ConvLSTM-LSTM deep learning model”, *Build. Environ.*, **239**, 110446. <https://doi.org/10.1016/j.buildenv.2023.110446>
- Xu, M. and Jin, D. (2024), “Prediction of the long-term deformation of high rockfill geostructures using a hybrid back-analysis method”, *Geomech. and Eng.*, **36**(1), 83–97. <https://doi.org/10.12989/gae.2024.36.1.083>